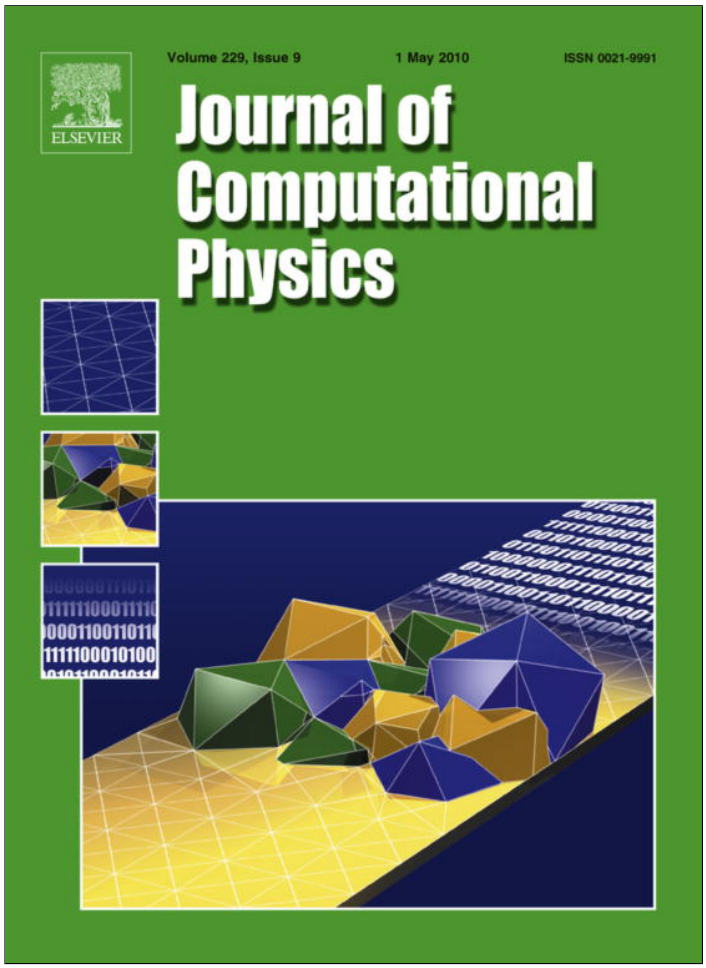

Journal of Computational Physics 229 (2010) 3121–3133

Contents lists available at ScienceDirect

Journal of Computational Physics

journal homepage: www.elsevier.com/locate/jcp

Pores resolving simulation of Darcy flows

Piotr K. Smolarkiewicz [a,*], C. Larrabee Winter [b]

[a] National Center for Atmospheric Research, Boulder, CO 80307, USA
[b] University of Arizona, Tucson, AZ 85721, USA

ARTICLE INFO

Article history:
Received 27 September 2009
Received in revised form 1 December 2009
Accepted 23 December 2009
Available online 4 January 2010

Keywords:
Darcy flows
Porous media
Immersed-boundary approach
Direct numerical simulation

ABSTRACT

A theoretical formulation and corresponding numerical solutions are presented for microscopic fluid flows in porous media with the domain sufficiently large to reproduce integral Darcy scale effects. Pore space geometry and topology influence flow through media, but the difficulty of observing the configurations of real pore spaces limits understanding of their effects. A rigorous direct numerical simulation (DNS) of percolating flows is a formidable task due to intricacies of internal boundaries of the pore space. Representing the grain size distribution by means of repelling body forces in the equations governing fluid motion greatly simplifies computational efforts. An accurate representation of pore-scale geometry requires that within the solid the repelling forces attenuate flow to stagnation in a short time compared to the characteristic time scale of the pore-scale flow. In the computational model this is achieved by adopting an implicit immersed-boundary method with the attenuation time scale smaller than the time step of an explicit fluid model. A series of numerical simulations of the flow through randomly generated media of different porosities show that computational experiments can be equivalent to physical experiments with the added advantage of nearly complete observability. Besides obtaining macroscopic measures of permeability and tortuosity, numerical experiments can shed light on the effect of the pore space structure on bulk properties of Darcy scale flows.

1. Introduction

Slow flow of an incompressible, viscous fluid through porous media is of interest to many areas of research and industry. Historically, computational efforts have focused on diagnosing steady macroscopic flows through inhomogeneous anisotropic media. Such flows are governed by stiff elliptic boundary value problems that result from imposing the mass-continuity constraint on the Darcy momentum flux with variable permeability; see [1,2] for examples. Regardless of their theoretical and practical importance, such efforts cannot (by design) address the influence of pore space geometry and topology on permeability – although the latter obviously depends on both. The actual permeability of a physical porous medium is hard to estimate from direct measurements of the geometry and topology of its pore space, and more often variations on Darcy's classic experiment are used to estimate permeability as a bulk property of a sample volume. Early numerical modeling of pore-scale flows tended to address the cumulative Stoke's drag on periodic arrays of idealized obstacles (viz. permeability of arrays [3]), and only recently advances in computational technology and in visualization of actual pore spaces have enabled progress with pore-scale simulation of percolating flows [4]. While the leading trend still is to simulate pore-scale transport with heavily reduced fluid equations, the harbingers of Navier–Stokes DNS [5–7] have already demonstrated the potential of virtual experiments for complementing laboratory studies.

* Corresponding author. Tel.: +1 303 497 8972; fax: +1 303 497 8181.
E-mail addresses: smolar@ucar.edu (P.K. Smolarkiewicz), lwinter@email.arizona.edu (C. Larrabee Winter).

0021-9991/$ - see front matter © 2009 Elsevier Inc. All rights reserved.
doi:10.1016/j.jcp.2009.12.031

In [7] the authors used X-ray computed tomography to tetrahedralise a scanned pore space and to generate an unstructured mesh for, perhaps the first ever, sensu-stricto DNS of steady incompressible Navier–Stokes flows through a real pore space. The results of numerical experiments were validated with the standard laboratory permeability test of a soil sample, demonstrating the equivalence to physical experiments with the added advantage of nearly complete observability. In spite of breaking the deadlock of "fundamental inability to describe the advection transport at the pore-scale" and demonstrating that "simulation with the Navier–Stokes equations mirrors results from Darcy's Law" [7], the technology involved still seems beyond the reach of many research groups, and the computational effort appears formidable (10 h of the wall-clock time to complete a simulation with $\sim 1.5 \times 10^6$ degrees of freedom). The latter is closely linked to the difficulties with representing geometrically complex boundaries, recognized as an obstacle for successful application of computationally efficient grid based methods [5].

In this paper we describe an alternative computational approach for simulating percolating flows with, in principle, arbitrary governing fluid equations in arbitrary pore spaces. Any virtual (computational) laboratory for pore-scale flow modeling requires two key ingredients: a method for prescribing pore space; and a method for representing relevant elements of fluid dynamics. As opposed to using natural specimens [7,8], which is usually limited to a small number of pore space samples that are difficult to observe, in this paper we generate random pore spaces via the statistical topography [9]. The latter method is technically simple, and advantageous when multiple realizations of a pore spaces are required. We implement the resulting porous media in the multi-scale computational fluid model EULAG – widely documented in the literature; see [10] for a recent review and a comprehensive list of references. The crux of our computational approach is the immersed-boundary (IMB) method – originated in the area of computational biomechanics [11,12] – that employs fictitious body forces in the equations of motion to mimic the presence of solid structures and internal boundaries[1]; see [15] for a review. The particular technique adapted is a variant of *feedback forcing* [16], with implicit time discretization admitting rapid attenuation of the flow to stagnation (within solid structures) in $\mathcal{O}(\Delta t)$ time comparable to the time step Δt of the fluid model. The efficacy of the IMB in EULAG has been verified by comparisons with solutions using boundary fitted coordinates and with wind tunnel data [17]. In spite of a broad range of documented IMB applications [18] – including flows past arrays of elemental bodies, e.g. [17,19,20] – there seems to be no significant record of simulating flows in realistic random porous media as addressed in [7]. Compared to the finite-element boundary fitted unstructured mesh model of [7] the approach proposed here is both simple and computationally undemanding – e.g. ~10 min of wall-clock time on 64 processors of the IBM Power6 machine to complete a simulation with $\sim 4.2 \times 10^6$ degrees of freedom. Nevertheless, it offers an effective means for analyzing flow through samples of simulated pore spaces. Besides mapping bulk properties like dependence of permeability on the porosity of the media and material properties of the fluid exactly from the simulations, the approach facilitates a study of the effect of pore space structure – given specified statistical details of pore space homogeneity and anisotropy, and topological properties like connectivity and grain size distributions – on bulk properties of Darcy scale flows.

The present paper is a pilot study on computational evaluation of pore scale flow in saturated and unsaturated porous media. Its goal is to introduce and validate the methodology underlying our virtual laboratory for studying multi-scale flows in porous media. With our emphasis on proof of concept – rather than on exhaustive study of pore space effects on macroscopic properties of porous media – the formulation of the pores resolving fluid model is discussed thoroughly in the next section. Numerical results are presented in Section 3, where we first analyze one canonical experiment in some detail, and then synthesize a series of simulations by giving sample results relating pore space properties to permeability.

2. Pores resolving fluid model

2.1. Theoretical formulation

The computational model EULAG accommodates a broad class of flows and underlying fluid equations, in a variety of domains on scales from laboratory and wind tunnel, through terrestrial environments and climate, to stellar [10]. Furthermore, EULAG is formulated in generalized time-dependent curvilinear coordinates to facilitate grid adaptivity to targeted flow features and/or irregular evolving boundaries [21–24]. Here, however, we integrate basic incompressible Navier–Stokes equations on a Cartesian domain with the linear scale $\mathcal{O}(10^{-2})$ m, thus dispensing with many complexities of EULAG's analytic formalism. Focusing on gravity-driven flows of a homogeneous incompressible fluid (e.g. water) through a porous medium, the adopted Navier–Stokes equations can be compactly written as

$$\begin{aligned} &\nabla \cdot \mathbf{v} = 0, \\ &d\mathbf{v}/dt = -\nabla \pi' + \mathbf{g}' + \nu \triangle \mathbf{v} - \alpha \mathbf{v}, \\ &d\boldsymbol{\delta}/dt = \mathbf{v}. \end{aligned} \tag{1}$$

Here, $d/dt = \partial/\partial t + \mathbf{v} \cdot \nabla$ is the total time derivative, with $\mathbf{v}$ denoting the velocity vector. The primes refer to perturbations with respect to static ambient atmospheric conditions characterized by a constant density ρ_o and pressure $p_o = p_o(z)$, so $\pi' = (p - p_o)/\rho$ and $\mathbf{g}' = (0, 0, -g\rho'/\rho)$, where $\rho = \text{const} \gg \rho_o$ denotes the density of water and g is the gravitational acceleration; the kinematic viscosity of water is denoted as ν. The last term on the right-hand-side (rhs) of the momentum

[1] Conceptually, this is in the spirit of statistical theories that treat the solid phase as an external force field constraining the fluid to the void space [13,14].

equation in (1) is the aforementioned repelling (fictitious) body force of the IMB method, with a non-negative time scale $\alpha^{-1}(\mathbf{x})$ and the corresponding inverse time scale $\alpha(\mathbf{x})$ that tend to vanish within the solid and fluid, respectively; its role and interpretation will be discussed shortly. The last equation in system (1) is merely supplemental, with the goal to facilitate analysis of the results. Here, $\boldsymbol{\delta}(\mathbf{x},t)=\mathbf{x}-\mathbf{x}_0$ is the Eulerian field of Lagrangian displacements of fluid particles with their initial location $\mathbf{x}_0=\mathbf{x}$, so $\boldsymbol{\delta}(\mathbf{x},t_0)=0$ everywhere.[2]

Relating the experimental Darcy's law [27] – the proportionality of a macroscopic mass flux and adverse pressure gradient – to basic principles of hydrodynamics is one of the classical problems in the study of flows in porous media. Consequently, the reproducibility of the law forms a key benchmark for microscopic theoretical/numerical models of percolating flows. In heuristic terms, Darcy's law relies on properties of a Poiseuille type flow within microscopic channels of the media (Section 4.8 in [28]), or on the Stokes' drag form of the effective resistive force of porous media on fluid parcels (Sections 4.7 and 5.10.4 in [29]). Theoretical derivations typically assume Stokes' incompressible creeping-flow equations – characterized by the balance between the body forces (e.g. gravity) and the divergence of the Navier–Stokes stress tensor – and proceed by homogenization of the resulting boundary value problem with no-slip conditions imposed at a random, multiply-connected fluid/solid interface [30–32]. The assumption of the Stokes' regime requires the characteristic scale of the pores $r \ll v/u$ (here u denotes a characteristic flow velocity; cf. Section 20 in [33]) tantamount to microscopic Reynolds number $Re = ru/v \ll 1$. With reasonable estimates of $v=\mathcal{O}(10^{-6})$ ms^{-2}, $r=\mathcal{O}(10^{-3})$m and $u=\mathcal{O}(10^{-3})$ ms^{-1}, this assumption is already violated. In (1) we relax the creeping-flow assumption, and admit problems with a broad range of hydraulic conductivities depending upon the media permeability and viscosity of the fluid.

The mathematical form of the repelling body force on the rhs of the momentum equation in (1) is reminiscent of the Stoke's drag. However, there is no physical connection between the two, as the former is merely a mathematical prerequisite of the numerical device circumventing the difficulty of imposing exact no-slip conditions along boundaries with complex geometry and topology. Intuitively, setting $\alpha(\mathbf{x})\equiv 0$ within the fluid admits Navier–Stokes flows away from the solid boundaries, while requiring $\alpha(\mathbf{x}) \nearrow \infty$ within the solid assures $\mathbf{v} \searrow 0$ there. Further estimates of the IMB efficacy can be derived by viewing the momentum equation in (1) as an abstract ODE along a flow trajectory

$$d\mathbf{v}/dt = \mathbf{f} - \alpha\mathbf{v}, \tag{2}$$

where $\mathbf{f}$ combines all physical forces. Its general solution (see Section IX.9 in [34]) can be written as

$$\mathbf{v} = \mathbf{v}_0 \exp\left[-\int_{t_0}^{t}\alpha(\tau)d\tau\right] + \int_{t_0}^{t}\mathbf{f}(s)\exp\left[-\int_{s}^{t}\alpha(\xi)d\xi\right]ds, \tag{3}$$

where the integrals are meant along the path $\mathbf{x}=\mathbf{x}_0+\int_{t_0}^{t}\mathbf{v}(\mathbf{x}(s))ds$, and $\mathbf{v}_0=\mathbf{v}(\mathbf{x}(t_0))$; within the fluid, (3) reproduces the formal path integral of the physical ODE $\dot{\mathbf{v}}=\mathbf{f}$. Keeping in mind that the goal is to resolve microscopic flow, the integration interval in (3) should be $t-t_0 \geqslant \mathcal{O}(\mathcal{T})$, with the microscopic characteristic time scale $\mathcal{T}=\max(r/u, r^2/v)$ accounting for both inertia and viscosity dominated flows (viz., large and small Re). On the other hand, a physically meaningful representation of the solid by means of the repelling forces demands

$$\alpha^{-1} \ll \mathcal{O}(\mathcal{T}) \leqslant t-t_0. \tag{4}$$

However, the accuracy and stability of numerical integrations of the governing problem in (1) necessarily require temporal increments $\Delta t \ll \mathcal{T}$, whereupon selecting $\alpha^{-1}=\mathcal{O}(\Delta t)$ assures (4). Assuming (for simplicity of the argument) $t-t_0=\mathcal{T}$ and $\alpha^{-1}=\text{const}$, (3) results in

$$\mathbf{v} = \mathbf{v}_0 e^{-\alpha\mathcal{T}} + \bar{\mathbf{f}}\alpha^{-1}(1-e^{-\alpha\mathcal{T}}), \tag{5}$$

where $\bar{\mathbf{f}}$ denotes mean value in the $t-t_0$ integration interval. Taking $\alpha^{-1}=\Delta t$ in (5) shows that within the solid the departures of flow velocity from stagnation are $\Delta\mathbf{v}=\mathcal{O}(\Delta t)$ over the microscopic scale $\mathcal{T}$, or $\Delta\mathbf{v}=\mathcal{O}(10^{-1}\Delta t)$ over the Δt increment of the numerical model. This generalizes the numerical analysis in appendix C of [17].

2.2. Numerical approximations

In EULAG all governing prognostic equations can be optionally integrated, on a regular computational grid,[3] as either Lagrangian evolution equations or Eulerian conservation laws [35,36]. Given that all calculations reported in this paper use exclusively the Eulerian option in a Cartesian-framework, each prognostic equation in (1) is idealized as

$$\frac{\partial\psi}{\partial t} + \nabla\cdot(\mathbf{v}\psi) = F, \tag{6}$$

where ψ symbolizes the components of $\mathbf{v}$ or $\boldsymbol{\delta}$, and F stands for the corresponding rhs. The governing system of the conservation laws (6) is integrated numerically using a second-order-accurate, semi-implicit, non-oscillatory forward-in-time (NFT) approach, whose theory, implementation and applications are broadly documented in [37–39] and references therein.

[2] The $\boldsymbol{\delta}(\mathbf{x},t)$ field should not be confused with particle tracking in either theoretical [13,14], experimental [25,26] or computational [5,6] models.

[3] Variability of physical mesh can be represented via continuous mappings [21–23].

All prognostic dependent model variables are co-located – a choice important for the efficacy of the semi-implicit integrals (cf. [17]) – so the resulting finite-difference approximations can be written compactly as

$$\psi_{\mathbf{i}}^{n+1} = \mathcal{A}_{\mathbf{i}}\left(\tilde{\psi}, \mathbf{v}^{n+1/2}\right) + 0.5\Delta t \mathcal{F}_{\mathbf{i}}^{n+1}. \tag{7}$$

Here: $\psi_{\mathbf{i}}^{n+1}$ is the solution sought at the grid point $(t^{n+1}, \mathbf{x}_{\mathbf{i}})$; $\tilde{\psi}_{\mathbf{i}} \equiv \psi_{\mathbf{i}}^{n} + 0.5\Delta t \mathcal{F}_{\mathbf{i}}^{n}$, with $\mathcal{F} = F + \mathcal{O}(\Delta x^2)$ symbolizing a centered spatial discretization of F; $\mathbf{v}^{n+1/2}$ is an $\mathcal{O}(\Delta t^2)$ estimate of the velocity at $t + 0.5\Delta t$; and $\mathcal{A}$ denotes a fully second-order-accurate two-time-level finite-volume NFT advection scheme. All calculations in this paper used the second-order-accurate monotone MPDATA scheme; already well reviewed in the literature [37,39,40].

For inviscid dynamics, all prognostic equations in (1) are integrated with (7) using, effectively, the trapezoidal rule and thus treating all forcings on the right-hand-side implicitly. Dissipative terms in the momentum equation are evaluated explicitly to $\mathcal{O}(\Delta t)$, and are included in $\mathcal{A}$. In technical terms, the definition of the auxiliary field $\tilde{\mathbf{v}}$ is expanded as $\tilde{\mathbf{v}} \equiv \mathbf{v}^n + 0.5\Delta t\left(\mathcal{F}_{inv}^n + 2\mathcal{F}_{vis}^n\right)$, while accounting only for the inviscid forcing $\mathcal{F}_{inv}$ in $\mathcal{F}^{n+1}$ on the rhs of (7). The explicit first-order evaluation of the dissipative forcing improves the efficacy of the calculations; however, when required, it can be extended to a trapezoidal integration by means of an outer iteration scheme [39].

Eq. (7) represents a system implicit with respect to pressure and all velocity components, because all principal forcing terms are assumed to be unknown at $n+1$. For the velocity vector $\mathbf{v}$, (7) is compactly written as

$$\mathbf{v}_{\mathbf{i}} = \tilde{\mathbf{v}}_{\mathbf{i}} - 0.5\Delta t(\nabla\pi' - \mathbf{g}' + \alpha\mathbf{v})_{\mathbf{i}}, \tag{8}$$

which can be readily written in the closed form

$$\mathbf{v}_{\mathbf{i}} = \hat{\mathbf{v}}_{\mathbf{i}} - 0.5\Delta t(1 + 0.5\Delta t\alpha_{\mathbf{i}})^{-1}\nabla_{\mathbf{i}}\pi', \tag{9}$$

where the explicit part $\hat{\mathbf{v}} = (\tilde{\mathbf{v}} + 0.5\Delta t\mathbf{g}')(1 + 0.5\Delta t\alpha)^{-1}$. Requiring the solution (9) to satisfy the mass-continuity constraint in (1) – discretized consistently with the divergence operator implied by $\mathcal{A}$ – leads to the discrete boundary value problem for pressure

$$\left\{\nabla \cdot \left[\hat{\mathbf{v}} - 0.5\Delta t(1 + \Delta t\alpha)^{-1}\nabla\pi'\right]\right\}_{\mathbf{i}} = 0. \tag{10}$$

The boundary conditions for $\nabla\pi' \cdot \mathbf{n}$ are implied by the boundary conditions imposed on $\mathbf{v}^{n+1} \cdot \mathbf{n}$ [21,22], subject to the integrability condition $\oint_{\partial\Omega} \mathbf{v}^{n+1} \cdot \mathbf{n}\, d^2x = 0$; here $\mathbf{n}$ denotes the outward unit normal to the boundary $\partial\Omega$ of the integration domain Ω. The resulting elliptic problem is solved using a preconditioned nonsymmetric Krylov-subspace solver [41,42]. Given the updated pressure, the updated velocity components are calculated from (9). Subsequently, the Lagrangian displacements $\boldsymbol{\delta}$ are updated according to (7).

Integrating the governing PDEs (1) as described has two important benefits relevant to this study. First, the implicit formulation of the model algorithm (7) evinces the optimal repelling time scale $\alpha^{-1} \equiv 0.5\Delta t$ (Appendix C in [17]), which automatically ensures that (4) is satisfied in calculations. Second, the nonlinear transport algorithm $\mathcal{A}$ suppresses spurious oscillations (notorious in linear discretizations) at sharp gradients of advected fields in vicinity of the fluid–solid interface. This not only improves the conditioning of the explicit part of the elliptic problem (and thus the solver's convergence), but it also facilitates simulations with substantially larger Reynolds number than for creeping-flow motions. Notably, the difficulties with representing geometrically complex boundaries – a weakness of computationally efficient grid based methods [5] – can be mitigated, given methods suitable for solving transport and elliptic problems with discontinuous dependent variables and random coefficients.

2.3. Virtual porous media

With the problem formulation and the method of its solution discussed in Sections 2.1 and 2.2, respectively, there appears to be no fundamental restriction on specifying the structure of virtual porous media admitted in our model. A realistic pore space can be designed based on X-ray computed tomography [7] as well as using a range of statistical methods [9]. Regardless of the structure of the media, the time scale $\alpha^{-1}(\mathbf{x})$ set to two distinct values in fluid and solid uniquely characterizes a realization of the media, while the governing equations admit a range of solutions from a free fall to global stagnation. To generate the pore space on a discrete model grid, we adopt an approach particularly undemanding from the perspective of massively-parallel self-contained numerical codes – albeit relating pore space properties to two basic parameters: the form of the convolution kernel and the level of the characteristic filter. Given a computational domain of $N_x \times N_y \times N_z$ grid points $\mathbf{i} = (\mathrm{i}, \mathrm{j}, \mathrm{k})$, a white-noise field $f_{\mathbf{i}}$ with values in the $[-0.5, 0.5]$ range is specified with a random-number generator. Next, with the aim to control the connectivity of the pore space and the size of individual pores/grains relative to grid resolution, the random field $f_{\mathbf{i}}$ is low-pass filtered using some m consecutive applications of the tensor product $f^{fflt} = f^{fltx} \otimes f^{flty} \otimes f^{fltz}$. Each alternate-direction application of the one-dimensional filter f^{fltx}, f^{flty} or f^{fltz} employs the trapezoidal rule integral over two adjacent grid boxes – e.g. $f_{\mathbf{i}}^{fltx} = 0.25(f_{\mathrm{i}+1,\mathrm{j},\mathrm{k}} + 2f_{\mathrm{i},\mathrm{j},\mathrm{k}} + f_{\mathrm{i}-1,\mathrm{j},\mathrm{k}})$ in the direction of x, with the amplitude response $\hat{f}^{fltx}(k) = \hat{f}(k)0.5(1 + \cos(k\Delta x))$, where k is the wave-number of the Fourier mode $\hat{f}(k)e^{ikx}$ on the grid. Such filtered field is then renormalized to assure that its values are in the $[-0.5, 0.5]$ range, and employed to generate a characteristic function of the pore space

$$\Lambda_{\mathbf{i}} = -1 \text{ if } f^{flt}_{\mathbf{i}} \leqslant \gamma \text{ and } \Lambda_{\mathbf{i}} = 1 \text{ otherwise.} \tag{11}$$

With the adopted convention that Λ takes respective values of -1 and 1 in void and solid, the limits of $\gamma \in [-0.5, 0.5]$ correspond to a solid block and an open channel. Fig. 1 illustrates this construction process with iso-surfaces of 3D white noise $f_{\mathbf{i}} = 0$, of filtered and renormalized field $f^{flt}_{\mathbf{i}} = 0$, and of the characteristic function $\Lambda_{\mathbf{i}} = 1$, for $m = 4$ and $\gamma = -0.025$ (in the interest of saving the journal space, the direction of gravity is from left to right).

The resulting porous medium shown in the lower panel of Fig. 1 is merely a geometric interpretation of the mathematical/numerical design. The governing system (1) senses the virtual pore space only via the inverse time scale of the repelling force α^{-1} defined as

$$\alpha_{\mathbf{i}} = 2/\Delta t \text{ if } \Lambda_{\mathbf{i}} > \varepsilon \text{ and } \alpha_{\mathbf{i}} = 0 \text{ if } \Lambda_{\mathbf{i}} < -\varepsilon, \tag{12}$$

where a small constant $\varepsilon > 0$ assures that the adopted definition is independent of the machine precision.

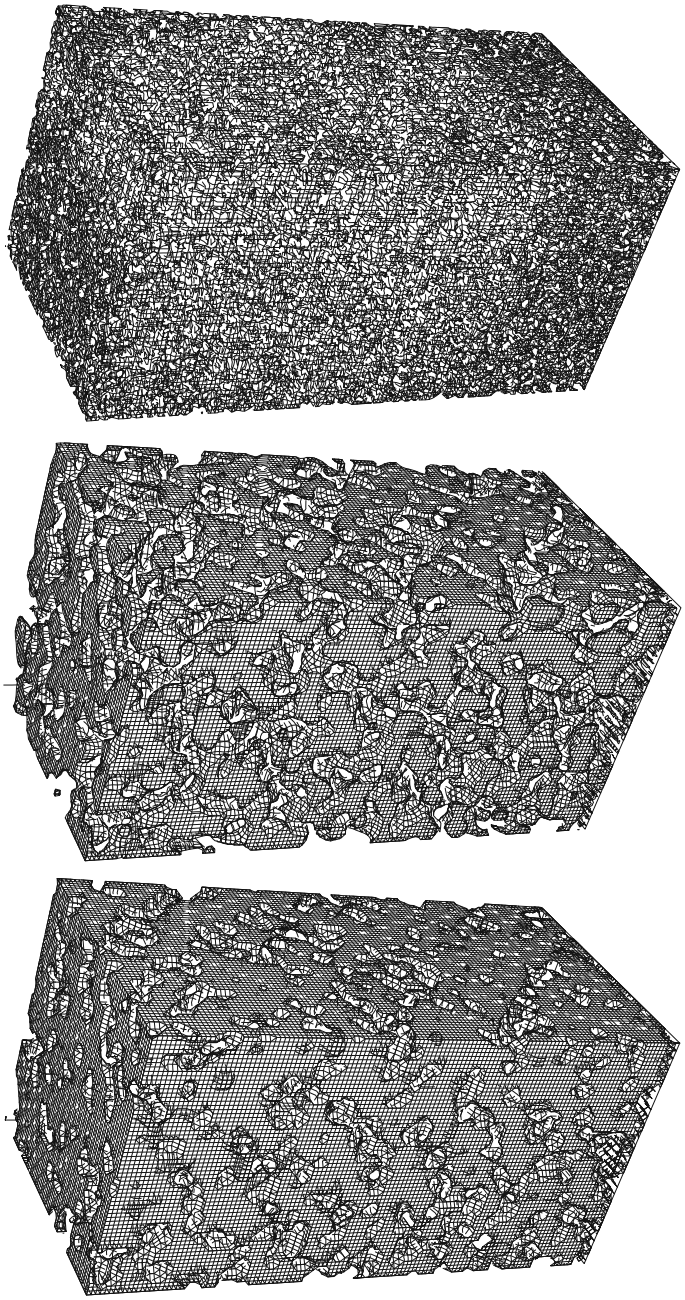

Fig. 1. Construction of random media, iso-surfaces of the generic and filtered noise and the characteristic pore space function (from top to bottom) in 1/8th of the actual model domain.

2.4. Design of experiments

A series of simulations is conducted for gravitationally driven flows in virtual porous media with different permeabilities corresponding to different values of level-set constant γ in the definition of characteristic function Λ. The initial flow is stagnant and all calculation are carried past a steady state, except for control free fall runs. The lateral boundaries are impermeable, whereas periodic boundaries are assumed in the vertical. The Cartesian model domain $L_x \times L_y \times L_z = 1.27 \cdot 10^{-2} \times 1.27 \cdot 10^{-2} \times 2.55 \cdot 10^{-2}$ m^3 is resolved with $N_x \times N_y \times N_z = 128 \times 128 \times 256$ points of the regular grid with uniform intervals $\Delta x = \Delta y = \Delta z = 10^{-4}$ m. All calculations span total time $T = t - t_0 = 5 \cdot 10^{-2}$ s with the increment $\Delta t = 5 \cdot 10^{-5}$ s.

The remaining simulation parameters are as follows. In (1), the reduced gravity $\mathbf{g}' = 0.999\,\mathbf{g}$ and the kinematic viscosity of water $\nu = 10^{-6}$ m^2 s^{-1} are assumed; and the inverse time scale of the repelling force $\alpha = 0.4 \cdot 10^5$ within the solid (recall that $\alpha \equiv 0$ in voids). Note that the characteristic time scales of the gravitational and viscous forces at the grid size – $(2\Delta z/g')^{1/2} = 4.5 \cdot 10^{-3}$ s and $\Delta z^2/\nu = 10^{-2}$ s, respectively – are two and three orders of magnitude larger than the repelling time scale $\alpha^{-1} = 0.5\Delta t = 2.5 \cdot 10^{-5}$ s. The total simulation time T is comparable to the time $(2L_z/g')^{1/2} = 7 \cdot 10^{-2}$ s of the free fall over the domain height L_z in the absence of solid grains (viz. $\alpha \equiv 0$ everywhere). On the other hand, T is also comparable to the time scale of viscous processes at the pore-scale. Thus, in all simulations, in which steady state solutions are attainable in a fraction of T, the results must be governed by the balance between the gravity and the grains' reaction force at the fluid/solid interface, with dissipation playing a minor role. Indeed this is verified by auxiliary inviscid calculations with $\nu \equiv 0$, exhibiting the same macroscopic behavior as in viscous runs (Section 3.2).

3. Numerical results

3.1. Reference simulation

The entire series of simulations specified in the preceding section aims at the mapping of macroscopic flow characteristics on properties of the porous media and vice versa. Before attempting such a synthesis of the series in next section, here we summarize the results of one selected experiment for the purpose of illustration, completeness and further reference.

The characteristic pore space function, Fig. 2, assumes $m = 4$ and $\gamma = 0$ in (11). The corresponding histogram, Fig. 3, of the vertical size of pores (normalized by Δz) documents a skewed distribution with the most frequent size at $2.6\Delta z$, roughly twice larger mean $6.3\Delta z$, and the standard deviation $4.7\Delta z$. To convey the skewed character of the distribution, later in the paper we shall refer to the *left* and *right* standard deviations – evaluated using the respective data to the left and right of the mean – with the sum of their squares equal the square of the standard deviation. For the case at hand, the left and right standard deviations are $2.7\Delta z$ and $3.8\Delta z$, respectively.

Fig. 4 shows the histories of the domain averaged vertical velocity and total speed $(\mathbf{v} \cdot \mathbf{v})^{1/2}$. After $t = 3 \cdot 10^{-2}$ s the averaged flow is essentially stationary, with mean vertical velocity $\langle w \rangle \approx -0.02$ ms^{-1} roughly twice larger than each horizontal component (assuming flow equipartition in each horizontal direction). Based on the value of $\langle w \rangle$ and the characteristic size of the pore space $r = \mathcal{O}(\Delta z)$, the miscroscopic Reynolds number $Re = r\langle w \rangle/\nu \approx 2$, clearly violating the creeping motion assumption ($Re \ll 1$), and thus motivating a posteriori the use of the Navier–Stokes equations in (1).

Fig. 5 complements the velocity histories in Fig. 4 with the histories of the domain averaged Lagrangian displacements. The solid line shows $|\delta_z| = \langle \delta_z^2 \rangle^{1/2}$, with δ_z denoting the vertical component of the displacement vector $\boldsymbol{\delta}$. Long and short dashes show, respectively, the value of the total displacement $|\boldsymbol{\delta}| = \langle \boldsymbol{\delta}^2 \rangle^{1/2}$ and a measure of its standard deviation $\sigma(|\boldsymbol{\delta}|) = \langle (\boldsymbol{\delta}^2 - \langle \boldsymbol{\delta}^2 \rangle)^2 \rangle^{1/4}$. All displacement values are normalized by the vertical domain size L_z. Consistent with the velocity histories, after $t = 3 \cdot 10^{-2}$ s the displacements grow linearly in time. The difference between the total and the vertical mean

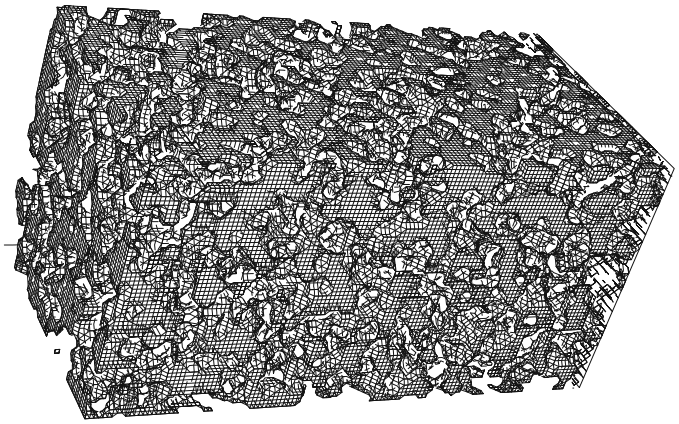

Fig. 2. Iso-surface of the characteristic pore space function used in the reference simulation with $m = 4$ and $\gamma = 0$; only 1/8th of the actual model domain is shown.

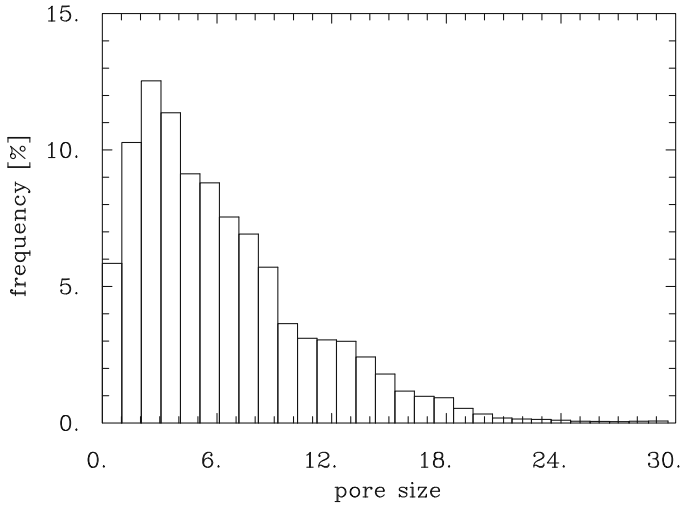

Fig. 3. Pore size frequency distribution, with the pore size normalized by the grid interval.

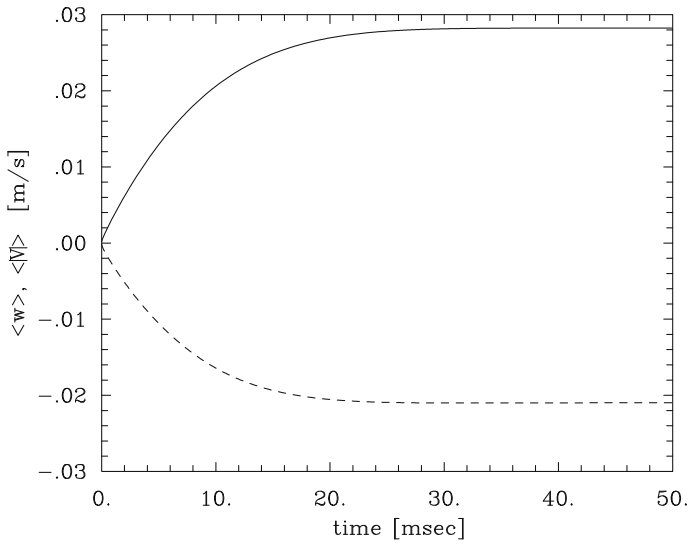

Fig. 4. Histories of the domain averaged vertical velocity $\langle w\rangle$ (dashed line) and total speed $|\mathbf{v}| = \langle\sqrt{\mathbf{v}^2}\rangle$ (solid line).

displacements are minuscule, indicating that the microscopic flow is predominantly vertical. The large value of the standard deviation measure (compared to the mean), indicates that the fluid is mostly blocked, so the flow must percolate throughout a relatively small number of long channels. This is illustrated by the display of instantaneous vertical velocity in the central xz plane in Fig. 6 that evinces only localized patches of the downward flow.

Fig. 7 shows the scatter plot of permeability κ in function of the model vertical coordinate, evaluated in voids as a ratio of the horizontally-averaged vertical velocity and pressure gradient

$$\kappa(z) = -\nu\overline{w}/\overline{\rho^{-1}\partial p'/\partial z}, \tag{13}$$

where the overline indicates horizontal average and $p' = p - p_o + g'\rho z$; see (1) and the accompanying discussion. For completeness, Fig. 7 also shows the average value $\langle\kappa\rangle = 0.97\cdot 10^{-8}$ m^2 (solid line) encompassed by the standard deviation $\sigma(\kappa)$ (dashed lines) and the least-square estimate $\kappa = 0.98\cdot 10^{-8}$ m^2 (long-dashed line). The latter was obtained by minimizing with respect to κ and c the functional $\mathcal{I}(\kappa, c) = \sum\left(-\kappa\overline{\rho^{-1}\partial p'/\partial z} + c - \nu\overline{w}\right)^2$, where the summation extends over all z-levels of the model. The proximity of the two estimates implies that the in voids fluctuations of $\overline{w}(z)$ and $\overline{\partial p'/\partial z}(z)$ are small compared to their vertically-averaged values, which is consistent with the data scatter in Fig. 7 roughly within 10% of the mean value. Consequently, the model predicted $\langle\kappa\rangle$ is a representative measure of the virtual porous medium shown in Fig. 2; its value corresponds to pervious materials like clean gravel, cf. Table 5.5.1 in [29].

3.2. Pore space effects on permeability

Here, we illustrate the potential of the proposed approach for studies of the effects that variations in pore space geometry and topology (e.g. connectivity, tortuosity, and porosity) have on macroscopic properties like permeability. In the following,

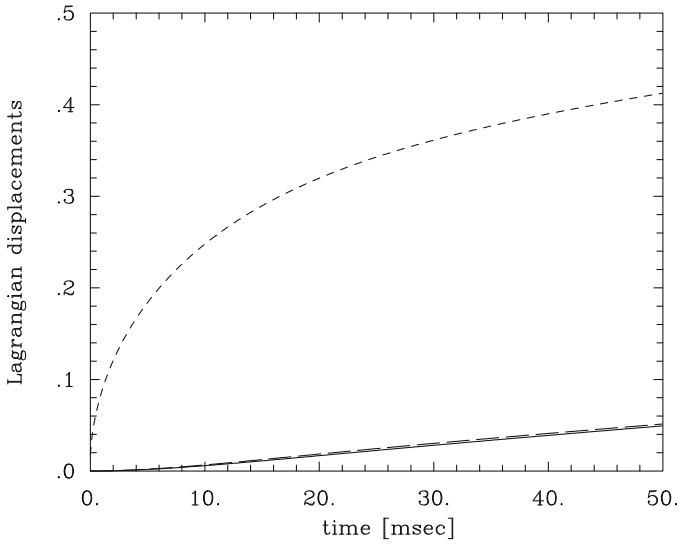

Fig. 5. Histories of the domain averaged Lagrangian displacements, normalized by the vertical domain size L_z. Solid line marks the vertical component, long dashes the total, and short dashes mark the standard deviation of the mean total displacement (see text for the definitions).

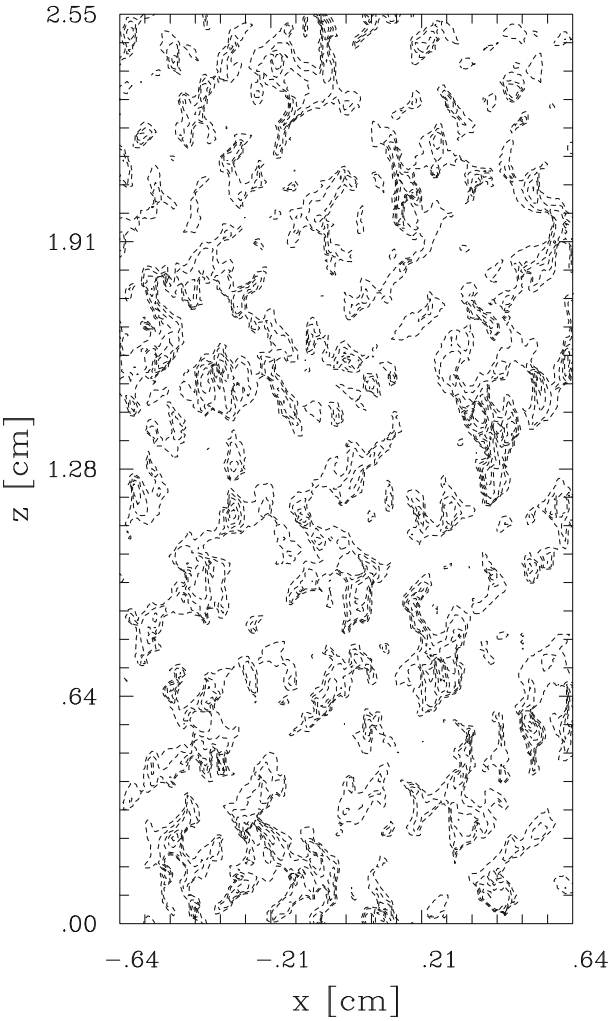

Fig. 6. Instantaneous vertical velocity in the central xz plane at $t = t_0 + 5 \cdot 10^{-2}$; contours in the range $[-18.75 \cdot 10^{-2}, -\Delta w]$ ms^{-1} are shown with the interval $\Delta w = 3.125 \cdot 10^{-2}$ ms^{-1}.

we synthesize two series of simulations. The first series consists of simulations like the reference simulation discussed in Section 3.1, but performed for a range of the level-set constant $\gamma \in [-0.15, 0.30]$ defining the discrete characteristic function of the pore space $\Lambda_{\mathbf{i}}$ in (11). The second series employs a much broader filter, $m = 16$, in the construction of the pore space;

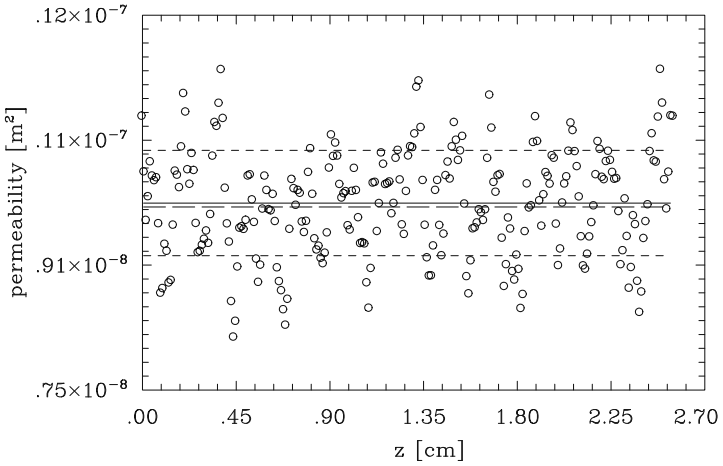

Fig. 7. Permeability; scatter plot together with the average value (solid line) encompassed by the standard deviation (short-dashed lines) and the least-square estimate (long-dashed line).

for illustration, compare Figs. 8 and 9 with Figs. 2 and 3. This second series complements the first one with less numerous calculations for $\gamma \in [-0.15, 0.15]$.

Figs. 10–12 summarize geometric properties of media used in the two series of simulations. Fig. 10 delineates the pore size frequency distributions in function of the level γ by depicting the mean (solid lines) encompassed by the left and right standard deviations (dotted-dashed lines underneath and above the mean, respectively). The data from the series with the narrower filter $m = 4$ are marked with circles, while crosses mark the $m = 16$ runs. An apparent effect of increasing the number of filter iterations (viz. the filter width) is admitting larger pores at the same γ, and thus increasing the effective model resolution. The corresponding values of porosity (the ratio of the void and total volumes, Fig. 11) span a range of plausible scenarios – from a solid rock at a lower end to a predominantly vacuous space surrounding a few embedded grains of solid; cf. Table 2.5.1 in [29]. Notably, Figs. 10 and 11 illustrate that media with statistically finer pores can have larger cumulative porosity.

Fig. 12 shows the domain averaged total Lagrangian displacements $|\boldsymbol{\delta}|$ corresponding to the final simulation time $t = t_0 + T$; cf. Fig. 5. Here, these normalized displacements are adopted as a measure of the media tortuosity factor; cf. Section 4.8.1 in [29]. Qualitatively, Figs. 12, 11 and 10 reflect that media tortuosity and porosity grow in concert with increasing size of pores (viz. with γ), which is an intuitively expected result. Quantitatively, Fig. 12 reveals distinct regimes of simulated flows and aids the interpretation of numerical results. The upper limit of the tortuosity factor at $\gamma = 0.3$ is 0.48. This value corresponds to the dimensional displacement $\delta_z = 0.48 L_z = 0.5$ g T^2; that is, the distance of the free fall over the total simulated time, anticipated at porosities approaching 100%. In the lower limit at $\gamma = -0.15$, the value $0.48 \cdot 10^{-3}$ corresponds to the dimensional distance $\delta_z = 12.24 \cdot 10^{-4}$ m $= 12.24 \Delta z = g' \alpha^{-1} T$; that is, the distance swept by the steady flow governed predominantly by the balance of gravity and the attenuating force $-g' - \alpha w = 0$ in (1). Indeed, the results equivalent to those in Fig. 4 (not shown) document that the flow becomes essentially steady within the first time step of the model. Both in the free fall and the balanced regime the flows are essentially vertical, Fig. 13, and neither regime corresponds to pore-resolving simulations of Darcy flows. We shall return to the discussion of these two regimes shortly.

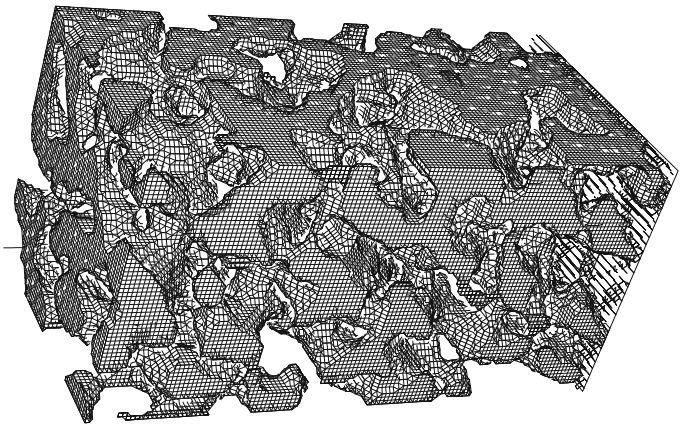

Fig. 8. Iso-surface of the characteristic pore space function in the simulation with $m = 16$ and $\gamma = 0$; cf. Fig. 2.

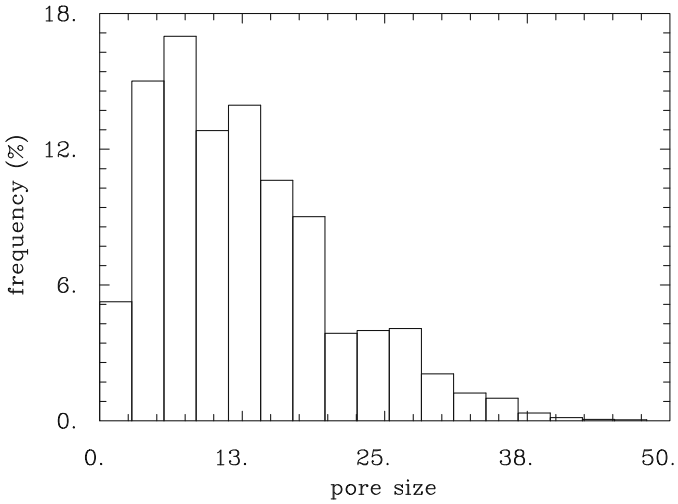

Fig. 9. Pore size frequency distribution, for $m = 16$ and $\gamma = 0$; cf. Fig. 3.

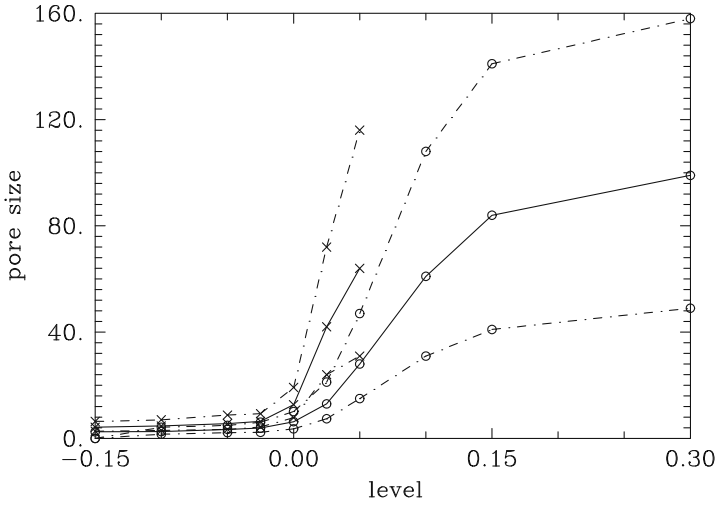

Fig. 10. Pore size statistics in function of γ; solid lines are for means, and dot-dashed lines for left and right standard deviations. Circles and crosses correspond to $m = 4$ and $m = 16$ filter iterations.

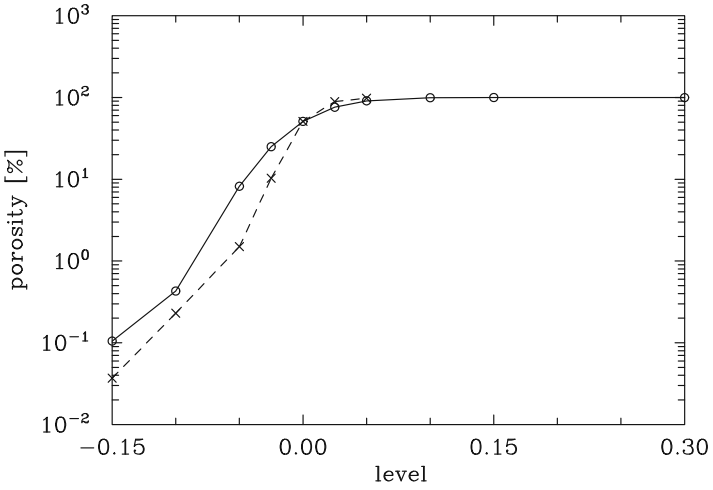

Fig. 11. Porosity in function of γ; circles and crosses correspond to $m = 4$ and $m = 16$ filter iterations.

With the approach adopted for generating virtual porous media (Section 2.3), at a given model resolution, the pore-resolving simulations are realized within a narrow region of the level-set constant $-0.05 \lesssim \gamma \lesssim 0.05$. This is substantiated by the dependence of the domain averaged permeability $\langle \kappa \rangle$ on γ in Fig. 14. A characteristic feature revealed by the figure

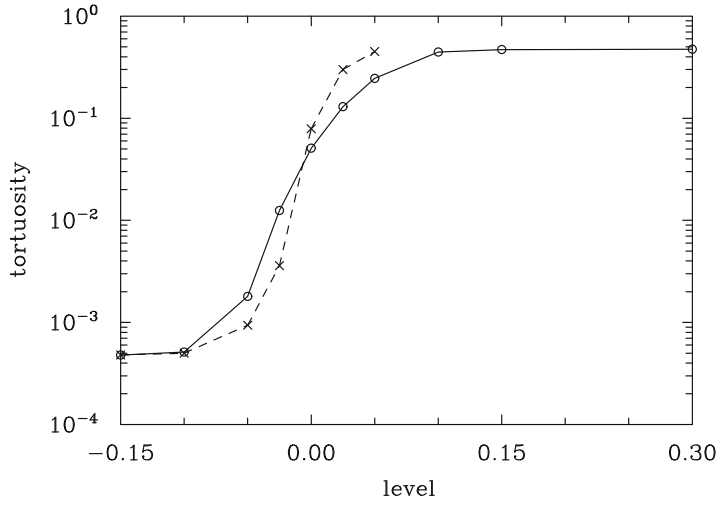

Fig. 12. Tortuosity measure $|\delta|$ at the final simulation time in function of γ; cf. Fig. 5.

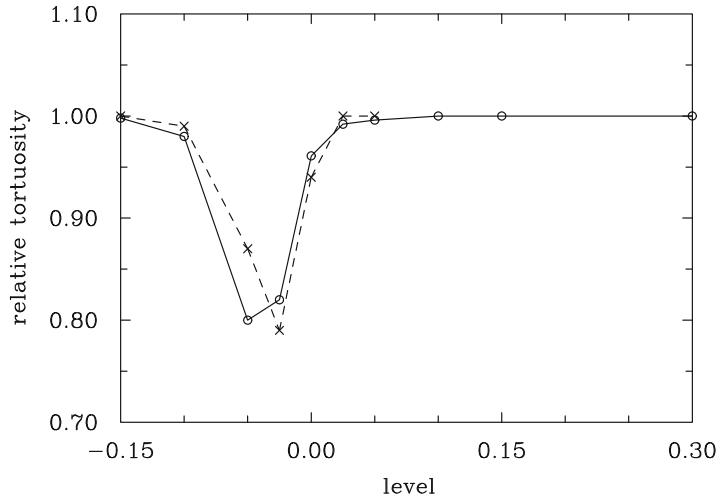

Fig. 13. The relative tortuosity measure $|\delta_z|/|\boldsymbol{\delta}|$ in function of γ, evaluated at the final simulated time.

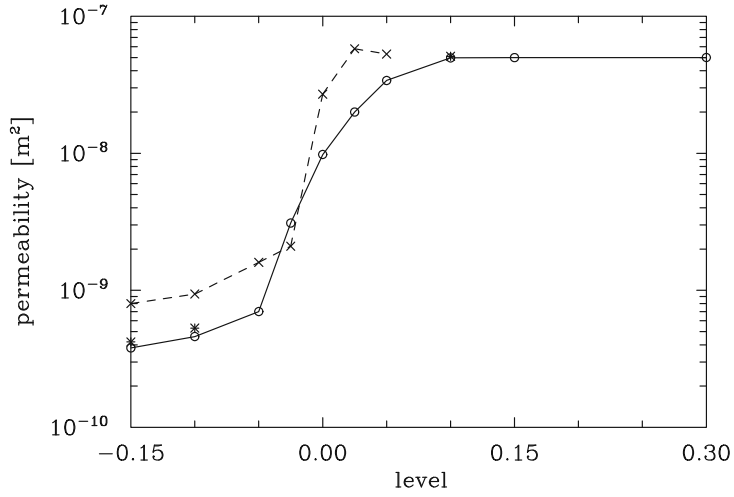

Fig. 14. Permeability $\langle\kappa\rangle(\gamma)$, evaluated at the final simulated time (cf. Fig. 7); asterisks are for $m = 4$ in (11) and $v = 0$ in (1).

is an abrupt increase of the permeability growth rate for $\gamma \geqslant -0.05$, tapered subsequently as $\gamma \nearrow 0.05$. This feature is concomitant with the increase of the tortuosity and of its horizontal counterpart, in particular. In contrast, the growth of the media porosity is more gradual. Altogether, this is symptomatic of the critical behavior of the hydraulic conductivity of the system near the percolation treshold $\gamma \approx -0.05$ [43]. Insofar as the numerical values of permeability are concerned,

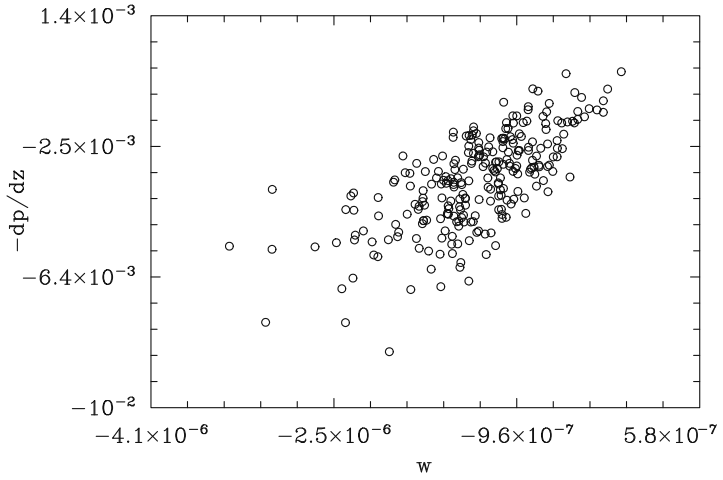

Fig. 15. Scatter plot of horizontally-averaged vertical component of pressure gradient force in voids $-\overline{\rho^{-1}\partial p'/\partial z}$ versus horizontally-averaged vertical velocity in voids $\overline{w}$, for $m = 4$ and $\gamma = -0.15$; the SI units are used.

for $-0.05 \lesssim \gamma \lesssim 0.05$ they all fall in the range of pervious materials, Table 5.5.1 in [29]. This does not imply the limitation of the approach to problems with high permeability, but merely reflects the particularity of the adopted experimental setup (Section 2.4). Either increasing the model resolution (both spatial and temporal) while keeping a realistically small size of pores, or increasing the viscosity would resolve flows with low permeability. Arguably, for $\gamma \lesssim -0.15$ the simulated flows fall in the transitional range of $Re \lesssim 1$, where viscous effects are relatively small and the inertial forces dominate (Fig. 5.3.2 in [29]). This is substantiated in Fig. 14 with the results of three additional control experiments at $m = 4$ and $\gamma = -0.15, -0.10$ and 0.10, for which the viscosity $\nu \equiv 0$ has been employed in the numerical integration of (1), but retained at the same value as for all other experiments ($\nu = 10^{-6}$ ms^{-2}) while evaluating the permeability in (13).

Outside the range of $-0.05 \lesssim \gamma \lesssim 0.05$ the calculations are still physically meaningful, but they represent different computational regimes than the targeted DNS of porous media flows. On the upper end, the calculations enter seamlessly the realm of large-eddy simulation (LES) of flows past complex bodies [17,24], thanks the implicit LES property of the employed non-oscillatory numerics [44,45]. More intriguing, on the lower end the calculations still capture some microscopic percolating flows. Given the balance of gravity and the repelling force ($-g' - \alpha w = 0$) in solid at small porosities, the domain averaged flow and the residual Lagrangian displacements are dominated by the truncation error estimated with (5). However, with $4.1 \cdot 10^6$ grid boxes even porosity as small as 0.1% leaves $4.1 \cdot 10^3$ void elements, within which the integration of the Navier–Stokes' equations proceeds. Fig. 15 shows the scatter plot of $-\overline{\rho^{-1}\partial p'/\partial z}$ versus $\overline{w}$ of the horizontally averaged values in voids, and it substantiates the significance of the resulting mean permeability $0.38 \cdot 10^{-9}$ m^2 (or $0.37 \cdot 10^{-9}$ m^2 when evaluated by the least-square fit). On the other hand, the lower end results reveal a complementary perspective. Because the balanced residual flow ($\langle w \rangle = 0.48 \cdot 10^{-3}$ m s^{-1}) dominates 99% of the model domain, the reduced geopotential $g'z$ becomes the dominant part of the pressure gradient force on the macro-scale. This implies the residual macro-scale permeability $\kappa_o = \nu/\alpha$ with numerical value $0.25 \cdot 10^{-10}$ m^2, and opens an entirely different avenue for the use of the repelling forces in modelling Darcy flows. Rather than simulating the porous media per se, the approach can be employed to model effective conductivity and permeability in the spirit of subgrid-scale parameterizations. Furthermore, both perspectives can be blended, possibly leading to seamless multi-scale modeling of natural flows in complex heterogeneous media.

Acknowledgments

Illuminating discussions with Douglas Nychka are gratefully acknowledged. The National Center for Atmospheric Research is sponsored by the National Science Foundation. This work was partially supported by the DOE award #DE-FG02-08ER64535.

References

[1] M.F. Wheeler, I. Yotov, A multipoint flux mixed finite element method, SIAM J. Numer. Anal. 44 (2006) 2082–2106.
[2] M.G. Edwards, H. Zheng, Double-families of quasi-positive Darcy-flux approximations with highly anisotrophic tensors on structured and unstructured grids, J. Comput. Phys. 229 (2010) 594–625.
[3] A.A. Zick, G.M. Homsy, Stokes flow through periodic arrays of spheres, J. Fluid Mech. 115 (1982) 13–26.
[4] M.I.J. van Dijke, M. Piri, Introduction to special section on modelling of pore-scale processes, Water Resour. Res. 43 (2007) W12S01.
[5] A.M. Tartakovsky, P. Meakin, Pore-scale modeling of immiscible and miscible fluid flows using smoothed particle hydrodynamics, Adv. Water. Resour. 29 (2006) 1464–1478.
[6] A.M. Tartakovsky, P. Meakin, T.D. Scheibe, R.M.E. West, Simulation of reactive transport and precipitation with smoothed particle hydrodynamics, J. Comput. Phys. 222 (2007) 654–672.

[7] W. Fourie, R. Said, P. Young, D.L. Barnes, The simulation of pore-scale fluid flow with real world geometries obtained from X-ray computed tomography, in: Proceedings of the COMSOL Conference 2007, Boston, <http://www.comsol.com/academic/papers/3039/>.
[8] Z.T. Karpyn, M. Piri, Prediction of fluid occupancy in fractures using network modeling and X-ray microtomography. I: data conditioning and model description, Phys. Rev. E 76 (2007) 016315.
[9] M.B. Isichenko, Percolation, statistical topography, and transport in random media, Rev. Modern Phys. 64 (1992) 961–1043.
[10] J.M. Prusa, P.K. Smolarkiewicz, A.A. Wyszogrodzki, EULAG, a computational model for multiscale flows, Comput. Fluids 37 (2008) 1193–1207.
[11] C.S. Peskin, Flow patterns around heart valves: a numerical method, J. Comput. Phys. 10 (1972) 252–271.
[12] C.S. Peskin, Numerical analysis of blood flow in the heart, J. Comput. Phys. 25 (1977) 220–252.
[13] J.H. Cushman, T.R. Ginn, Nonlocal dispersion in media with continuously evolving scales of heterogeneity, Trans. Porous Media 13 (1993) 123–138.
[14] J.H. Cushman, M. Moroni, Statistical mechanics with three-dimensional particle tracking velocimetry experiments in the study of anomalous dispersion. I.Theory, Phys. Fluids 13 (2001) 75–80.
[15] R. Mittal, G. Iaccarino, Immersed-boundary methods, Ann. Rev. Fluid Mech. 37 (2005) 239–261.
[16] D. Goldstein, R. Handler, L. Sirovich, Modeling a no-slip flow boundary with an external force field, J. Comput. Phys. 105 (1993) 354–366.
[17] P.K. Smolarkiewicz, R. Sharman, J. Weil, S.G. Perry, D. Heist, G. Bowker, Building resolving large-eddy simulations and comparison with wind tunnel experiments, J. Comput. Phys. 227 (2007) 633–653.
[18] S. Kang, G. Iaccarino, F. Ham, DNS of buoyancy-dominated turbulent flows on a bluff body using the immersed-boundary method, J. Comput. Phys. 228 (2009) 3189–3208.
[19] R. Dillon, L. Fucci, A microscale model of bacterial and biofilm dynamics in porous media, Biotechnol. Bioeng. 68 (2000) 536–547.
[20] Q. Liu, O.V. Vasilyev, A Brinkman penalization method for compressible flows in complex geometries, J. Comput. Phys. 227 (2007) 946–966.
[21] J.M. Prusa, P.K. Smolarkiewicz, An all-scale anelastic model for geophysical flows: dynamic grid deformation, J. Comput. Phys. 190 (2003) 601–622.
[22] N.P. Wedi, P.K. Smolarkiewicz, Extending Gal-Chen and Somerville terrain-following coordinate transformation on time dependent curvilinear boundaries, J. Comput. Phys. 193 (2004) 1–20.
[23] P.K. Smolarkiewicz, J.M. Prusa, Towards mesh adaptivity for geophysical turbulence: continuous mapping approach, Int. J. Numer. Meth. Fluids 47 (2005) 789–801.
[24] P. Ortiz, P.K. Smolarkiewicz, Coupling the dynamics of boundary layers and evolutionary dune, Phys. Rev. E 79 (2009) 041307.
[25] M. Moroni, J.H. Cushman, Statistical mechanics with three-dimensional particle tracking velocimetry experiments in the study of anomalous dispersion. II. Experiments, Phys. Fluids 13 (2001).
[26] M. Moroni, A. Cenedese, J.H. Cushman, Application of 3D-PTV to track passive scalars in porous media, Trans. Porous Media 79 (2009) 43–65.
[27] H. Darcy, Les Fountains Publiques de la Ville de Dijon, Dalmont, Paris, 1856.
[28] G.K. Batchelor, An Introduction to Fluid Dynamics, Cambridge University Press, 1967. 615 pp..
[29] J. Bear, Dynamics of Fluids in Porous Media, American Elsevier Publishing Company, 1972. 764 pp..
[30] S.P. Neuman, Theoretical derivation of Darcy's law, Acta Mech. 25 (1977) 153–170.
[31] S. Whitaker, Flow in porous media I: a theoretical derivation of Darcy's law, Trans. Porous Media 1 (1986) 3–25.
[32] F. Rubinstein, S. Torquato, Flow in random porous media: mathematical formulation, variational principles, and rigorous bounds, J. Fluid Mech. 206 (1989) 25–46.
[33] L.D. Landau, E.M. Lifshitz, Fluid Mechanics, Elsevier, 2004. 539 pp..
[34] K. Maurin, Analysis Part I: Elements, Reidel Publ. Comp., 1976. 430 pp..
[35] P.K. Smolarkiewicz, J.A. Pudykiewicz, A class of semi-Lagrangian approximations for fluids, J. Atmos. Sci. 49 (1992) 2082–2096.
[36] P.K. Smolarkiewicz, L.G. Margolin, On forward-in-time differencing for fluids: extension to a curvilinear framework, Mon. Weather Rev. 121 (1993) 1847–1859.
[37] P.K. Smolarkiewicz, L.G. Margolin, MPDATA: a finite-difference solver for geophysical flows, J. Comput. Phys. 140 (1998) 459–480.
[38] P.K. Smolarkiewicz, J.M. Prusa, Forward-in-time differencing for fluids: simulation of geophysical turbulence, in: D. Drikakis, B.J. Guertz (Eds.), Turbulent Flow Computation, Kluwer Academic Publishers, Dordrecht, 2002, pp. 279–312.
[39] P.K. Smolarkiewicz, J. Szmelter, Iterated upwind schemes for gas dynamics, J. Comput. Phys. 228 (2009) 33–54.
[40] P.K. Smolarkiewicz, Multidimensional positive definite advection transport algorithm: an overview, Int. J. Numer. Methods Fluids 50 (2006) 1123–1144.
[41] P.K. Smolarkiewicz, V. Grubišić, L.G. Margolin, On forward-in-time differencing for fluids: stopping criteria for iterative solutions of anelastic pressure equations, Monthly Weather Rev. 125 (1997) 647–654.
[42] P.K. Smolarkiewicz, C. Temperton, S.J. Thomas, A.A. Wyszogrodzki, Spectral Preconditioners for nonhydrostatic atmospheric models: extreme applications, in: Preceedings of the ECMWF Seminar Series on Recent Developments in Numerical Methods for Atmospheric and Ocean Modelling, 6–10 September 2004, Reading, UK, pp. 203–220.
[43] B. Berkowitz, I. Balberg, Percolation approach to the problem of hydraulic conductivity in porous media, Trans. Porous Media 9 (1992) 275–286.
[44] J.A. Domaradzki, Z. Xiao, P.K. Smolarkiewicz, Effective eddy viscosities in implicit large eddy simulations of turbulent flows, Phys. Fluids 15 (2003) 3890–3893.
[45] L.G. Margolin, P.K. Smolarkiewicz, A. Wyszogrodzki, Dissipation in Implicit turbulence models: a computational study, ASME J. Appl. Mech. 73 (2006) 469–473.